Received: 21 October 2021 | Revised: 11 March 2022 | Accepted: 26 March 2022 | Published on: 16 May 2022

DOI: 10.1002/qj.4284

Quarterly Journal of the Royal Meteorological Society RMetS

RESEARCH ARTICLE

The relationship between precipitation and its spatial pattern in the trades observed during EUREC^{4}A

Jule Radtke[1,2] | **Ann Kristin Naumann**[1,3] | **Martin Hagen**[4] | **Felix Ament**[1,3]

[1]Meteorological Institute, Center for Earth System Research and Sustainability, Universität Hamburg, Hamburg, Germany

[2]International Max Planck Research School on Earth System Modelling, Max Planck Institute for Meteorology, Hamburg, Germany

[3]Max Planck Institute for Meteorology, Hamburg, Germany

[4]Deutsches Zentrum für Luft- und Raumfahrt, Institut für Physik der Atmosphäre, Oberpfaffenhofen, Germany

Correspondence
J. Radtke, Meteorological Institute, Universität Hamburg, Hamburg 20146, Germany
Email: jule.radtke@uni-hamburg.de

Funding information
Deutsche Forschungsgemeinschaft (DFG, German Research Foundation) under Germany's Excellence Strategy—EXC 2037 'CLICCS—Climate, Climatic Change, and Society', Grant/Award Number: 390683824

Abstract

Trade wind convection organises into a rich spectrum of spatial patterns, often in conjunction with precipitation development. Which role spatial organisation plays for precipitation and vice versa is not well understood. We analyse scenes of trade-wind convection scanned by the C-band radar Poldirad during the EUREC^{4}A field campaign to investigate how trade-wind precipitation fields are spatially organised, quantified by the cells' number, mean size, and spatial arrangement, and how this matters for precipitation characteristics. We find that the mean rain rate (i.e., the amount of precipitation in a scene) and the intensity of precipitation (mean conditional rain rate) relate differently to the spatial pattern of precipitation. Whereas the amount of precipitation increases with mean cell size or number, as it scales well with the precipitation fraction, the intensity increases predominantly with mean cell size. In dry scenes, the increase of precipitation intensity with mean cell size is stronger than in moist scenes. Dry scenes usually contain fewer cells with a higher degree of clustering than moist scenes do. High precipitation intensities hence typically occur in dry scenes with rather large, few, and strongly clustered cells, whereas high precipitation amounts typically occur in moist scenes with rather large, numerous, and weakly clustered cells. As cell size influences both the intensity and amount of precipitation, its importance is highlighted. Our analyses suggest that the cells' spatial arrangement, correlating mainly weakly with precipitation characteristics, is of second-order importance for precipitation across all regimes, but it could be important for high precipitation intensities and to maintain precipitation amounts in dry environments.

KEYWORDS

field campaign, observations, precipitating shallow convection, spatial organisation, trade wind regime

1 | INTRODUCTION

The trades are raining. This fact is, however, given minimal attention in many studies of the trades (e.g., Rieck *et al.*, 2012; Siebesma *et al.*, 2003; Stevens, 2005). Trade wind convection is typically described as non-precipitating and randomly distributed "popcorn" convection (e.g., Betts, 1997; Siebesma, 1998; Stevens, 2005). Since the trade-wind

region and its clouds, important to cool our Earth, emerged as central to the issue of climate change because they dominate the spread in climate sensitivity among climate models (e.g., Bony and Dufresne, 2005; Vial *et al.*, 2013), new studies have proven this description to be wrong. Field studies and satellite imagery have emphasised how trade-wind convection organises into a rich spectrum of spatial patterns, often in conjunction with precipitation development (Schulz *et al.*, 2021; Snodgrass *et al.*, 2009; Stevens *et al.*, 2020). This raises the question of the role of spatial organisation for precipitation and vice versa. To address this question, this study investigates the spatial behaviour of precipitating shallow convection and how it matters for precipitation characteristics in the trades.

A fair part of the motivation for our study dates back to the Rain In Cumulus over the Ocean (RICO) field campaign (Rauber *et al.*, 2007). RICO showed that shallow precipitation is common in the trades, with about one-tenth of the cloudy areas raining (Nuijens *et al.*, 2009; Snodgrass *et al.*, 2009). Other studies estimate that warm rain showers contribute 20–30% to the total precipitation amount over tropical oceans and 70% to the total precipitation area (Lau and Wu, 2003; Short and Nakamura, 2000). Precipitation might be key to understand the vertical thermodynamic structure, cloudiness, and spatial organisation of the trade regime (e.g., Vogel *et al.*, 2016). Controls on precipitation in shallow convection, however, remain poorly constrained and the representation of precipitation in large eddy simulations differs largely (vanZanten *et al.*, 2011). An understanding of how spatial organisation influences precipitation rates might help interpret and reduce these differences (Stevens *et al.*, 2021).

Besides quantifying precipitation rates, the RICO campaign highlighted that precipitation was often observed with arc-shaped cloud patterns associated with cold-pool outflows (Snodgrass *et al.*, 2009; Zuidema *et al.*, 2012). These cold-pool signatures reflect how precipitation links processes acting on different scales. The evaporation of precipitation on the microscale can induce cold pools (Seifert and Heus, 2013; Touzé-Peiffer *et al.*, 2022) and local circulations on the mesoscale, which can trigger the birth of new convective cells and pattern the convection. These local circulations may change the characteristics of clouds, and therefore also precipitation formation. Precipitation, convection, and their spatial patterns or organisation are thus highly intertwined. Understanding their interplay could be crucial for a better understanding of the individual processes. In turn, to better understand their interplay, a view from the different individual perspectives might be needed.

However, recent studies have mainly focused on the perspective of clouds and their spatial patterns (e.g., Bony *et al.*, 2020; Denby, 2020; Rasp *et al.*, 2020). An investigation from the perspective of precipitation on its interaction with spatial organisation and an analysis of precipitation patterns in the trades is lacking. Which role spatial organisation plays for precipitation and vice versa is poorly understood. Bony *et al.* (2020) show that cloud patterns differ in their cloudiness and net radiative effect. How do precipitation characteristics relate to precipitation patterns in the trades? For the case of deep convection, using a storm-resolving model, Brueck *et al.* (2020) found that mesoscale tropical precipitation varies independently from the spatial arrangement of its convective cells. Louf *et al.* (2019), investigating radar observations in the Tropics, found that rainfall intensities are strongest for few large cells. How does shallow convection differ from deep convection or resemble it in these relationships?

To address our questions, we investigate scenes of trade-wind convection scanned by the C-band polarization diversity radar (Poldirad; Hagen *et al.*, 2021) during the EUREC^{4}A field campaign (Stevens *et al.*, 2021), which took place in January and February 2020 in the western tropical North Atlantic near Barbados. In these scenes, we analyse how trade-wind precipitation fields are organised into spatial patterns and how this relates to the scenes' precipitation amount and intensity. While the amount of precipitation is related to the scene heating and drying (e.g., Nuijens *et al.*, 2009), the intensity of precipitation is important in a local sense for the triggering of cold pools, for example (Snodgrass *et al.*, 2009). Spatial organisation is not straightforward to define, and different metrics weight different attributes. We jointly analyse three attributes to investigate the spatial pattern into which trade-wind precipitating convection is organised: the number, size, and spatial arrangement of cells. Given the relationship between water vapour, precipitation, and organisation found in earlier studies (e.g., Bretherton and Blossey, 2017; Nuijens *et al.*, 2009), we further include vertically integrated water vapour as measured by Global Navigation Satellite System (GNSS) receivers (Bock *et al.*, 2021) during EUREC^{4}A as a supplementary variable in our analysis.

The data and methods used in this study are described in Section 2. First, we investigate the spatial organisation in trade-wind precipitation fields (Section 3) by analysing the number, size, and spatial arrangement of rain cells and how they covary (Section 3.1). Second, we show how the moisture environment of rain cells relates to their spatial behaviour and identify two moisture regimes (Section 3.2). With this information, we then analyse and interpret the relationship between the cells' spatial organisation and the amount and intensity of precipitation in Section 4. Finally, we show how the relationship between precipitation and

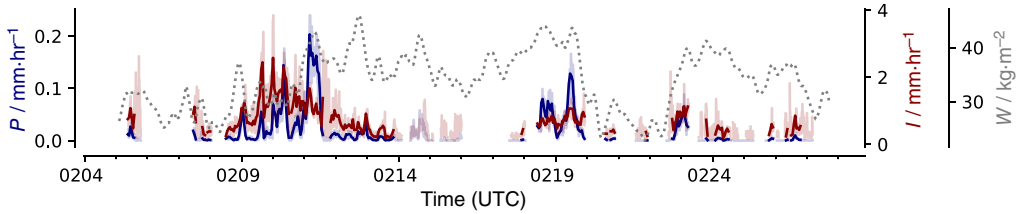

FIGURE 1 Time series of precipitation amount P, precipitation intensity I (thick lines display hourly means of the dataset used in the analysis, shading full dataset), and integrated water vapour W [Colour figure can be viewed at wileyonlinelibrary.com]

its spatial pattern behaves in the diurnal cycle (Section 5), before we conclude in Section 6.

2 | DATA AND METHODOLOGY

2.1 | EUREC⁴A field campaign

EUREC⁴A was designed to elucidate the coupling between clouds, circulation, and convection (Bony *et al.*, 2017). The field campaign took place in January and February 2020 in the western tropical Atlantic, with most operations based out of the island of Barbados and targeting a comprehensive observation of clouds, precipitation, and their atmospheric and oceanic environment in the trades upwind of Barbados. A thorough overview of EUREC⁴A is provided in Stevens *et al.* (2021). Here, we exploit observational data from the C-band radar Poldirad that was deployed on Barbados to provide a detailed view of the upstream precipitating trade-wind convection (Hagen *et al.*, 2021). Furthermore, we include observations of vertically integrated water vapour from GNSS receivers (Bock *et al.*, 2021) at the Barbados Cloud Observatory (Stevens *et al.*, 2016).

2.1.1 | C-band research radar Poldirad

Poldirad is a polarimetric C-band research radar of the German Aerospace Center (Schroth *et al.*, 1988). During EUREC⁴A, Poldirad took long-range surveillance scans at a 5 min schedule with a maximum range of 375 km in a sector of about 100° eastward and upwind of Barbados, thus mapping out the spatial distribution of rain cells in the trade-wind region. Here, we use the gridded data interpolated on a $1 \times 1\,\mathrm{km}^2$ grid with a size of $400 \times 400\,\mathrm{km}^2$ from these long surveillance scans and covering the month of February (Figure 1). This dataset and the radar's deployment in the EUREC⁴A field campaign are described in detail in Hagen *et al.* (2021). For our analyses we examine the scans between the 25 and 175 km range (see Figure 2) as the radar beam remains below about 3 km height up to this range and the frequency of strong echoes is approximately constant, and to limit effects of sea clutter. To discriminate between meteorological echoes and non-meteorological echoes (like sea clutter, vessels, aircraft, and other targets), a threshold in the copolar correlation coefficient ρ_{HV} was applied (see Hagen *et al.*, 2021).

The dataset by Hagen *et al.* (2021) provides a rain rate derived from the commonly used Z–R relationship $Z = 200R^{1.6}$ (Marshall *et al.*, 1955). Here, we use another Z–R relationship, $Z = 148R^{1.55}$, as in Nuijens *et al.* (2009), which is specifically derived for shallow precipitation. Differences in the Z–R relationship lead to uncertainties in the absolute estimation of rain rates, which, however, is not the aim of this study and a shortcoming we accept for this paper. Please also note that peaks in rainfall are smoothed by the radar beam and the gridding, resulting in lower absolute rain rates. Additionally, the Poldirads' radar beams showed an elliptical shape that caused the cells to appear stretched in the azimuthal direction, resulting in an overestimation of the size of the rain cells. For an estimation of this effect, please see Hagen *et al.* (2021, appendix A).

For each scene scanned by the radar, we calculate the precipitation amount P (rain rate averaged across the entire scene, which includes non-precipitating and precipitating areas) and precipitation intensity I (rain rate averaged across the precipitating area only), whereby $P = I \cdot F$ and F is the rain fraction. To give an overview of the dataset, Figure 1 shows the time series of both P and I. Gaps in a continuous operation are caused by failures and limited personnel resources. In our subsequent analyses we exclude radar scans from the period February 13–15 because not only shallow cloud systems were present and captured by the radar at this time (Villiger *et al.*, 2022). We also exclude all scans with less than five precipitating cells as a characterisation of the spatial arrangement is difficult for scenes with few objects. The dataset captures maxima in P up to roughly $0.2\,\mathrm{mm\cdot hr^{-1}}$, which compares well to precipitation amounts observed in the RICO campaign (Nuijens *et al.*, 2009), and values of I up to roughly $4\,\mathrm{mm\cdot hr^{-1}}$. Please note that the dominant relationships

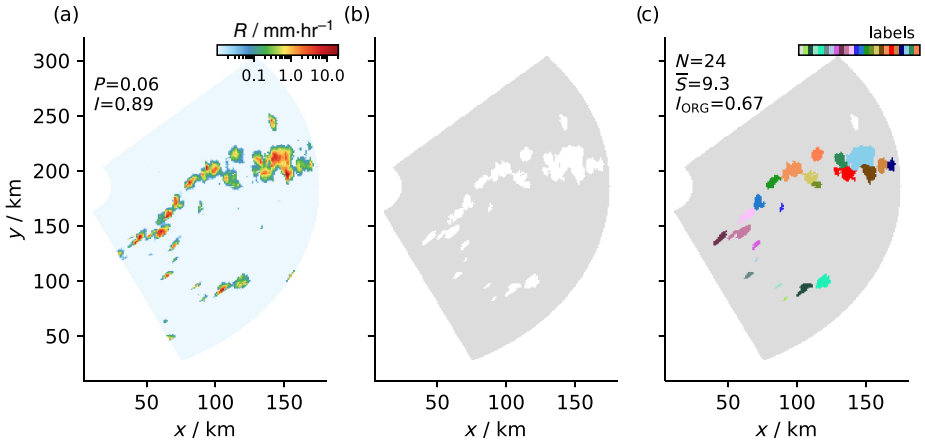

FIGURE 2 Example scene of (a) rain rate, (b) rain mask, and (c) rain cell segmentation from February 11, 2020, 0050 h. For symbols, see text [Colour figure can be viewed at wileyonlinelibrary.com]

between precipitation characteristics and spatial organisation that we show in the following are qualitatively similar when we consider only independent scenes; that is, only about every 6 hr.

2.1.2 | Integrated water vapour observations

To analyse the moisture environment of the rain cells, we use integrated water vapour W observations from GNSS receivers (Bock *et al.*, 2021) installed at the Barbados Cloud Observatory. This dataset provides high temporal resolution integrated water vapour measurements at a 5 min time interval. To provide an estimate of W for the scenes scanned by the radar to the east, we shift the time series of W by 100 km (i.e., to the scene centre approximately) assuming a mean wind speed of 6 $m \cdot s^{-1}$ and smooth the time series with a running mean of 100 km/6 $m \cdot s^{-1}$ to account for a field mean. The integrated water vapour field is rather smooth, so that changes in the interpolation details do not lead to substantial differences. According to Nuijens *et al.* (2009), most of the variability in moisture, when conditioned on precipitation, is in the lower free troposphere. The time series of W is also shown in Figure1.

2.2 | Identification of rain cells and derivation of their spatial attributes

To identify the rain cells that populate each scene, we follow Brueck *et al.* (2020). We use a lower threshold of 0.1 $mm \cdot hr^{-1}$ (i.e., ~7 dBZ) to define a rain mask that segments precipitating objects from their non-precipitating environment. The rain cells are derived by a two-dimensional watershed segmentation technique based on the local precipitation maxima. To detect the local maxima, the precipitation field is first smoothed with a multidimensional Gaussian filter with a standard deviation for the Gaussian kernel of 1. The filtering is not applied to, and does not affect, the precipitating area and rate. The local maxima are detected by using a maximum filter. This dilates the image. If a pixel is unchanged following this dilation (i.e., the dilated image equals the original image), then that pixel is a local maximum. The local maxima serve as starting points for the watershed procedure. In this procedure, the precipitating neighbourhood surrounding a local maximum is filled until it gets into contact with another neighbourhood. Owing to possible regridding artefacts, we only consider rain cells of minimum two pixel size. Furthermore, we exclude rain cells that touch the scene boundary. Figure 2 shows the segmentation for one exemplary scene.

After the segmentation procedure, we calculate for each scene the cells' geometrical properties size, number, and distance between cells. From these, we derive the attributes that we will use to analyse the organisation of trade-wind precipitation fields into spatial patterns. Size, number, and distance are common ingredients in metrics of spatial organisation; for example, in the Simple Convection Aggregation Index (Tobin *et al.*, 2012), the Convective Organisation Potential (White *et al.*, 2018), or the Radar Organisation Metric (Retsch *et al.*, 2020). Depending on the metric, certain spatial properties are weighted more heavily than others. Therefore, rather than focusing on just one metric, we choose to investigate three attributes of spatial organisation together, based on the number, size, and spacing between cells.

For each scene, we derive the mean cell size $\overline{S}$, which we express in terms of the area equivalent diameter to provide a length scale similar to the distances between the cells. We will provide an overview of the individual cell sizes and show how the mean cell size scales with the distribution of cell sizes in a scene in Section 3. The product of mean cell size expressed in terms of the area $(\pi/4) \cdot \overline{S}^2$ and the number of cells N equals the precipitating area

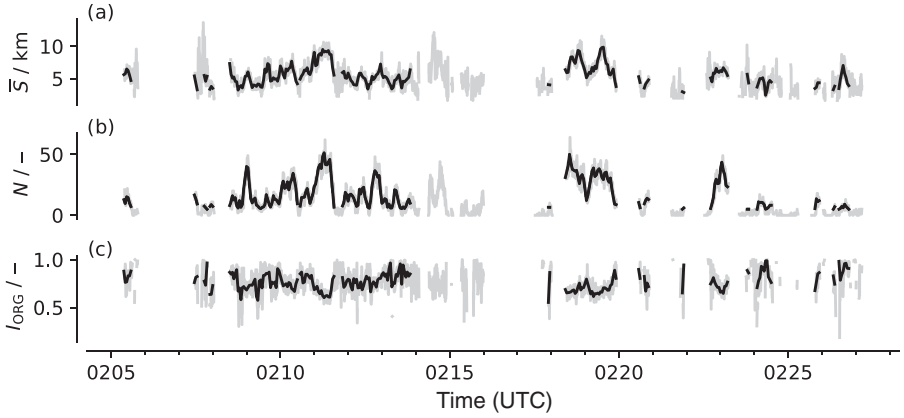

FIGURE 3 Time series of (a) mean cell size $\overline{S}$, (b) number of cells N and (c) the spatial arrangement of cells quantified by I_{ORG} (thick lines display hourly means of the dataset used in the analysis, shading full dataset)

$A = F \cdot A_{scene}$ with F the rain fraction and A_{scene} the scene area. The first two measures, $\overline{S}$ and N, hence inform about the spatial composition of the precipitation area. We will use this relationship in our analyses. The time series of $\overline{S}$ and N are shown in Figure 3a,b.

To assess the spatial arrangement of cells, we use the index I_{ORG} (Tompkins and Semie, 2017; Weger *et al.*, 1992). Please note that the naming of I_{ORG} might be misleading here, as we consider spatial arrangement as only one attribute of spatial organisation. I_{ORG} is a metric of spatial arrangement based on nearest-neighbour distances and compares the observed distances between the cells with the distances of a random distribution with the same number of cells. If nearest-neighbour distances are on average smaller than expected from a random distribution, the cells are considered clustered, otherwise they are regularly distributed. The time series of I_{ORG} is shown in Figure 3c. Formally, I_{ORG} is defined as the integral below the curve of the cumulative density function of the actual observed nearest-neighbour distances (NNCDF) plotted against the NNCDF for a random distribution of the cells. A value of 0.5 corresponds to a random distribution, values larger than 0.5 indicate clustering, whereas values smaller than 0.5 indicate regularly distributed cells. To obtain the random distribution of distances for our domain size, we follow Brueck *et al.* (2020) and randomly distribute disks with the same areas and same number as the cells present in the scene domain. The random distribution results from taking the mean over 100 realisations of this procedure. As a consistency check, we investigated a second metric of spatial arrangement based on the distances between all possible pairs of cells (Tobin *et al.*, 2012), which compares the observed mean all-neighbour distance with the random mean all-neighbour distance. Both metrics show the same relationships, so that we only show I_{ORG} in the remainder of this article. Please also note that the dominant relationships between precipitation characteristics and spatial arrangement remain similar when using a different threshold on the number of cells; for example, considering only scenes with at least 15 or 20 cells.

The time series in Figure 3 indicate that $\overline{S}$, N, and I_{ORG} do not vary independently from each other. $\overline{S}$ and N often tend to increase and decrease together, and decreases in I_{ORG} (towards a more regular distribution of rain cells) tend to go along with increases in N; for example, on February 11 or 19 . Figure 4 provides an overview of the correlations between $\overline{S}$, N, I_{ORG}, P, and I across the whole dataset. As indicated by the time series, $\overline{S}$ and N are positively correlated. The I_{ORG} and N are negatively correlated and I_{ORG} and $\overline{S}$ are weakly negatively correlated. In the following, we will work our way from top to bottom in Figure 4. We will first look more closely at $\overline{S}$, N, and I_{ORG} and investigate and interpret how and why they covary (Section 3). To do so, we will span a phase space of $\overline{S}$ and N, following analyses in deep convection studies (Brueck *et al.*, 2020; Louf *et al.*, 2019). We will use this phase space in our subsequent analyses to interpret the correlations shown in Figure 4 in more detail. Analysing organisation and precipitation in the phase space will help us to identify two moisture regimes (Section 3.2), show that competing effects lead to the weak correlation of P and I with I_{ORG} (Section 4), and that I predominantly increases with $\overline{S}$, but that this increase differs with the moisture regime.

3 | HOW ARE TRADE-WIND PRECIPITATION FIELDS SPATIALLY ORGANISED?

3.1 | Number, size, and spatial arrangement

Figure 2 shows a scene with a mean cell size $\overline{S}$ of about 9 km and cell sizes ranging between 2.8 and 20.7 km. Therewith, the scene is exemplary for a large mean rain cell size during EUREC^{4}A (Figure 3a) and represents well the range of observed cell sizes (Figure 5a).

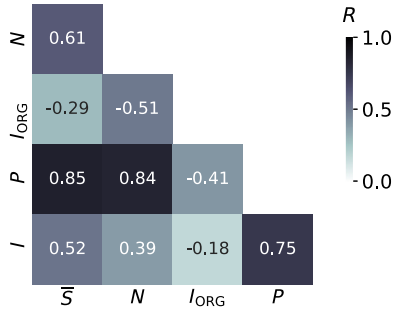

FIGURE 4 Spearman correlation coefficient R between cell number N, mean cell size $\overline{S}$, the cells' spatial arrangement quantified by I_{ORG}, precipitation amount P, and precipitation intensity I, coloured according to the absolute correlation between a variable pair [Colour figure can be viewed at wileyonlinelibrary.com]

Figure 5a shows that a cell size larger than 20 km was rarely observed. The slope of the distribution of cell sizes falls off towards high cell sizes. This was similarly noted by Trivej and Stevens (2010) for precipitation cells in the RICO campaign. About 50% of the cells have a size smaller than 5 km, and 10% of the cells have a size larger than 10 km. We investigate how the mean cell size relates to the individual cell sizes in a scene. Figure 5b shows that the maximum cell size and spread in cell sizes, quantified as the interquartile range of cell sizes, increase with the mean cell size. Both are strongly correlated with the mean cell size with correlation coefficients of 0.89 and 0.83, respectively. This suggests that a few cells drive the growth in mean cell size. Processes that trigger this growth for a few cells thus probably have a dominant role; for example, the merging of cells or colliding cold pools that trigger large rain cells.

The joint frequency of occurrence of mean cell size $\overline{S}$ and cell number N is shown in Figure 6. The example scene contains 24 cells (Figure 2), which is exemplary for a moderate rain cell number N during EUREC^{4}A. About 60% of scenes contained less than 20 cells, and most frequently the scenes contained a small cell number between 5 and 15, and a mean cell size of around 5 km. Figure 6 shows that N and $\overline{S}$ are positively correlated with a correlation coefficient of 0.61 (Figure 4). In radar scans measuring the number and size of rain cells in deep tropical convection, no positive correlation was found (Darwin radar observations; Louf *et al.*, 2019). In these observations, the largest cell sizes occur for small cell numbers, whereas in our analyses the largest cell sizes occur for large cell numbers (Figure 6). The difference between Darwin and EUREC^{4}A possibly reflects a difference between shallow and deep convection. In deep convection, large cells likely induce local circulations that suppress the growth of other cells around them. Our analyses suggest that this may not always happen in shallow convection. Given their positive correlation, the phase space of $\overline{S}$ and N spanned here, which we will use in our subsequent analysis, allows us to examine the relationship of a variable with cell number separately from the relationship of the same variable with cell size.

In the example scene (Figure 2), the cells are distributed at an average distance of 70 km (L_A) or 15 km if only the distance to the nearest neighbour is taken into account (L_{NN}). Figure 7a,b shows how these two properties, L_A and L_{NN}, varied during EUREC^{4}A and that L_A and L_{NN} in the example scene are typical observed distances. Most frequently an L_A around 65 km and L_{NN} around 14 km were observed. The distribution of L_{NN} is unimodal and skewed towards higher L_{NN} (Figure 7b). L_{NN} varies only in a narrow range; that is, rain cells have a typical

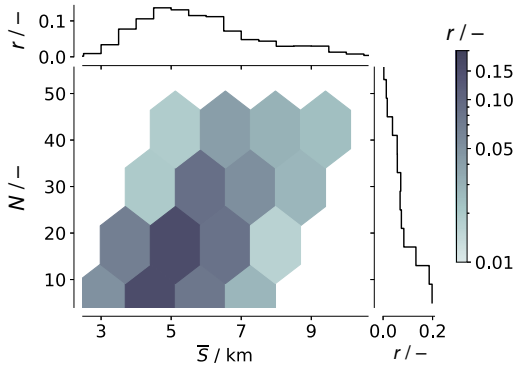

FIGURE 6 Joint relative frequency of occurrence of mean cell size $\overline{S}$ and number of cells N with individual histograms [Colour figure can be viewed at wileyonlinelibrary.com]

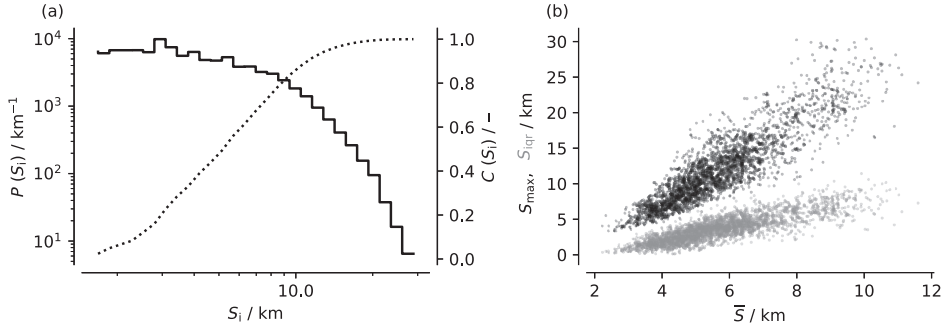

FIGURE 5 (a) Distribution of cell sizes $P(S_i)$ (solid line) and cumulative distribution of cell sizes $C(S_i)$ (dashed line). (b) Maximum cell size S_{max} (dark colour) and cell size spread, quantified as the interquartile range of cell sizes S_{iqr} (light colour), as a function of mean cell size $\overline{S}$ per scene

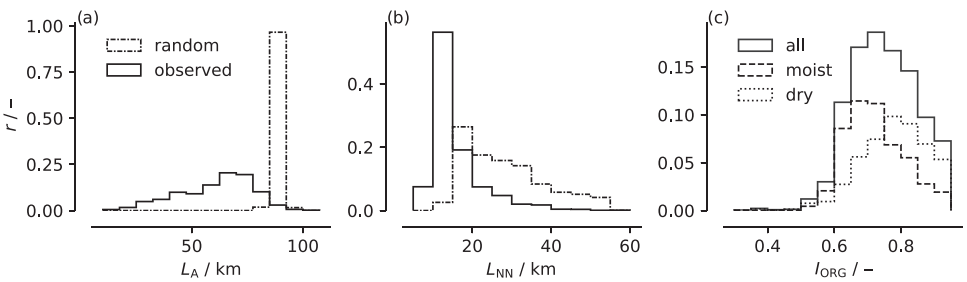

FIGURE 7 Relative frequency of (a) mean distance between all possible pairs of cells L_A, (b) mean distance between nearest-neighbour cells L_{NN}, and (c) the I_{ORG} for all, dry ($W <$ median (W)), and wet scenes ($W >$ median (W)) with median (W) = 36 kg·m^{-2}

distance to their neighbouring cell. The distribution of L_A shows a less marked peak and is skewed towards small L_A (Figure 7a). Possibly, cold pools (e.g., visible in Figure 2 with the typical arc-shaped pattern) smooth and widen the distribution of L_A by their varying strength and extent.

If the rain cells in the example scene were randomly distributed, L_A would be around 90 km and L_{NN} around 19.5 km. That is, the observed distances are shorter than the random distances, and the scene in Figure 2 shows a clustered state, which is classified by an I_{ORG} of 0.67 (Figure 2). As indicated in Figure 7a,b and shown in Figure 7c, the rain cells' arrangement is clustered in almost all scenes ($I_{ORG} > 0.5$). This was similarly found in studies of deep convection (e.g., Brueck *et al.*, 2020; Pscheidt *et al.*, 2019). That precipitation fields are usually clustered fits with the idea that precipitation processes develop in cloud complexes with several clustered updrafts and representing inhomogeneities. Precipitation does not occur randomly but due to inhomogeneities in a field, and therewith clustered.

We now analyse how the cells' spatial arrangement, cell number, and size covary by analysing the I_{ORG} in the $\overline{S}$–N phase space spanned before (Figure 8a). The analysis reveals three main findings. First, few cells (small N) are more clustered (higher I_{ORG}) than many cells (high N). For a given $\overline{S}$, I_{ORG} decreases with N. That is, clustering and cell number are negatively correlated ($R = -0.51$, Figure 4). Brueck *et al.* (2020), noting the same relationship, point to thermodynamic considerations that can help explain this behaviour. When conducting idealised simulations, in a scene starting from homogeneous thermodynamic conditions it can be seen that many randomly distributed cells appear, whereas in the presence of inhomogenities the number of cells in a scene can be limited. By subsampling the scenes into four composites representing the four corners of the $\overline{S}$–N phase space (Figure 9) to show the variability in each composite, we further note that scenes with few cells have a wider range of possible spatial arrangements than scenes with many cells do (Figure 9c). In particular, few and small cells, indicative of little precipitation, occur in a variety of spatial arrangements, which

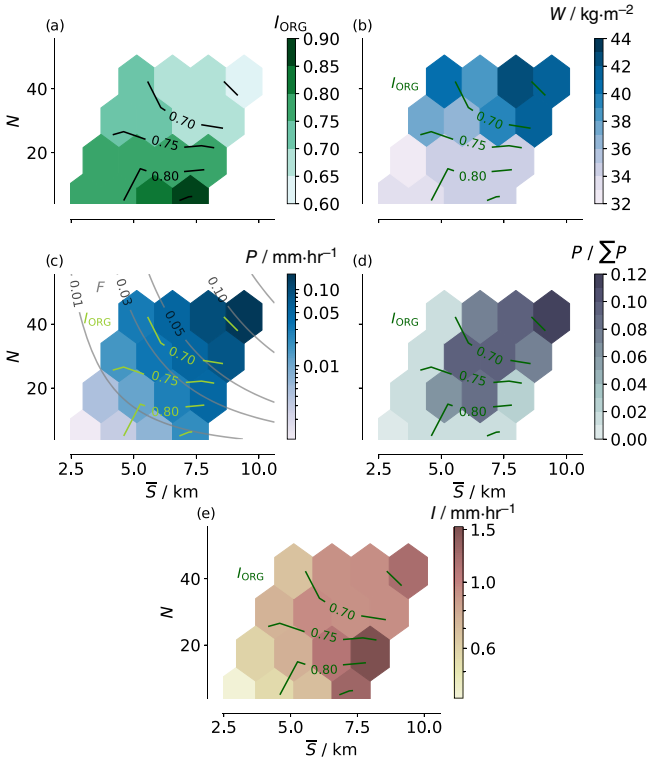

FIGURE 8 (a) I_{ORG}, (b) integrated water vapour W, (c) precipitation amount P, (d) contribution to total precipitation $P/\sum P$, and (e) precipitation intensity I as a function of mean cell size $\overline{S}$ and cell number N [Colour figure can be viewed at wileyonlinelibrary.com]

fits the subjective analysis of radar and satellite imagery during the RICO campaign (Rauber *et al.*, 2007).

Second, the covariability of clustering with cell size is more complex than with cell number. Whereas I_{ORG} increases with $\overline{S}$ in scenes with a small N, I_{ORG} decreases with $\overline{S}$ in scenes with a large N (Figure 8a). Thus, overall, the correlation between $\overline{S}$ and I_{ORG} is weak ($R = -0.29$, Figure 4). Third, I_{ORG} consequently maximises in the lower right corner of the $\overline{S}$–N phase space (Figure 8a); that is, clustering is typically highest where cells are few and on average large (see also Figure 9c). This was similarly found for deep tropical convection (Brueck *et al.*, 2020; Retsch

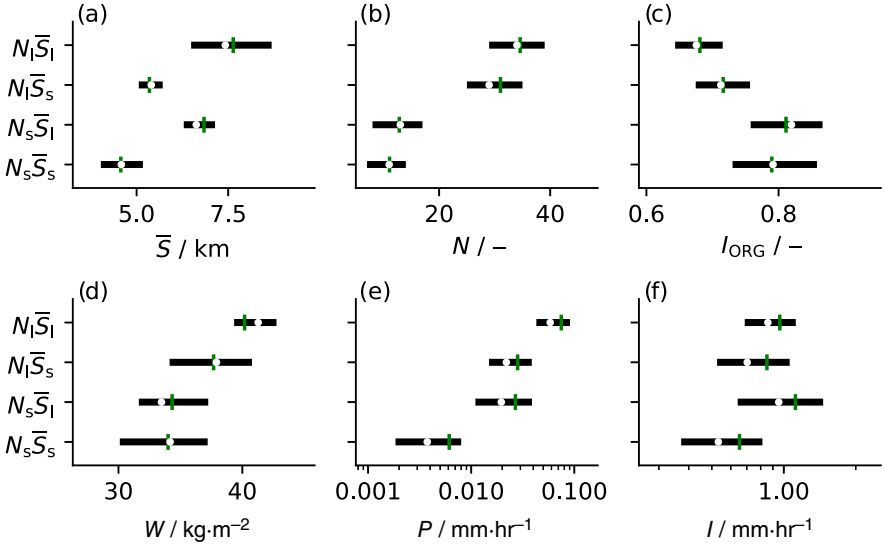

FIGURE 9 Interquartile range (black box), median (white dot) and mean (green line) of mean cell size $\overline{S}$, cell number N, and I_{ORG} for four composites representing the four corners in the $\overline{S}$–N phase space with $N_s < 20$, $N_l > 20$, $\overline{S}_s < 6$ km, $\overline{S}_l > 6$ km. The number of scenes is equal in each composite [Colour figure can be viewed at wileyonlinelibrary.com]

et al., 2020). In Brueck *et al.* (2020), the degree of clustering increases with mean cell size at all cell numbers. The difference between shallow and deep convection might be explained by the idea that deep convective precipitation often originates from large precipitating systems, where large cells are part of a large convective object and hence clustered, whereas trade wind showers can also be associated with less organised precipitation systems, as suggested by the gravel cloud pattern (Stevens *et al.*, 2020). Nevertheless, our analysis suggests that the organisation of precipitation in trade-wind shallow convection shares similarities to deep convection, in that clustering and cell number are negatively correlated and the degree of clustering is typically highest in scenes containing few and, on average, large cells. Next, we will show how the different scaling of I_{ORG} with $\overline{S}$ in regimes of small and large N is related to different moisture regimes.

3.2 | Moisture environment

Past studies have shown that water vapour path is related to precipitation (e.g., Bretherton *et al.*, 2004; Nuijens *et al.*, 2009) as well as organisation (e.g., Bretherton *et al.*, 2005;Tobin *et al.*, 2012). Investigating W in the $\overline{S}$–N phase space (Figure 8b), we find that the scenes are on average driest (low W) at small N and $\overline{S}$ and moistest (high W) at large N and $\overline{S}$. With a moistening of the environment, cells tend to be larger and more numerous. However, whereas W increases markedly with N for a given $\overline{S}$, the increase of W with $\overline{S}$ for a given N is weak. For a large cell number, W tends to increase with $\overline{S}$; but for a small cell number, W varies weakly with $\overline{S}$. Differences in the water vapour path thus mainly appear in the number of rain cells and only slightly in the mean size of the cells. Therefore, the $\overline{S}$–N phase space shows predominantly two regimes: a moist regime (high W) at high cell number and a dry regime (low W) at low cell number. That dry and moist scenes differ predominantly in the number of cells they contain, whereas the mean area of the cells only varies weakly with W, was also found in radar observations (Louf *et al.*, 2019) and simulations (Brueck *et al.*, 2020) of deep convection. In a moist environment, clouds may be less affected by entrainment, which allows them to reach deeper and eventually start to precipitate (Smalley and Rapp, 2020). Also, clouds, and hence precipitating cells, may live longer in moister environments. Both could explain the enhanced cell numbers in moist compared with dry environments. That large cells also exist in dry environments could be related to clustering.

We now investigate how the moisture environment and the degree of clustering are related. A comparison of W and the I_{ORG} in the $\overline{S}$–N phase space (Figure 8b) shows that scenes with a small cell number are typically drier and show a higher degree of clustering than scenes with a large cell number (see also Figure 9d). Figure 7c displays the histogram of I_{ORG} in moist versus dry scenes ($W \lesseqgtr$ median (W) with median $(W) = 36$ kg·m^{-2}). In dry scenes, the distribution shifts towards a higher degree of clustering. This agrees with idealised studies of radiative convective equilibrium (Bretherton *et al.*, 2005; Muller and Held, 2012) and observations (e.g., Tobin *et al.*, 2012), which show that aggregated or clustered states of deep convection are typically drier. Our analyses show the same for shallow convection. Possibly, isolated rain cells, that is with a low degree of clustering, can hardly exist in dry environments as they are strongly affected by entrainment. Clustering might reduce the updraft buoyancy reduction through entrainment, allowing cells to develop in hostile, dry environments (Becker *et al.*, 2018).

4 | HOW DOES SPATIAL ORGANISATION MATTER FOR PRECIPITATION CHARACTERISTICS?

4.1 | Precipitation amount

First, we analyse how precipitation amount varies as a function of cell size and number. Figure 8c shows that, for a given $\overline{S}$, P increases with N; and vice versa, for a given N, P increases with $\overline{S}$. Taken together, contours of P follow well the contour lines of rain fraction F. For the amount of precipitation, the intensity of rain showers is hence of secondary importance, which is in agreement with previous studies (e.g., Nuijens *et al.*, 2009). Because precipitation amount scales very well with precipitating fraction, P is strongly correlated with $\overline{S}$ and N ($R \approx 0.85$, Figure 4). Consequently, precipitation amounts can be similar for scenes with few and on average large cells or scenes with many and on average small cells, given a similar rain fraction, and scenes with numerous and on average large cells exhibit usually the highest precipitation amount (Figure 9e).

We note two implications from the relationship of P with N and $\overline{S}$. First, although scenes with a mean cell size of ∼5 km and small cell number occur most frequently, they do not contribute the most to the total precipitation during EUREC^{4}A (Figure 8d). Figure 8d shows that the precipitation contribution is shifted to larger and more numerous cells compared with the frequency distribution (Figure 6). Although they occur rarely, scenes with the largest and most numerous cells do contribute the most to the total precipitation, because of their high rain amount. Additionally, a moderate cell size and number contribute substantially to the total precipitation through a combination of a moderate rain rate and moderate frequency of occurrence.

Second, as $\overline{S}$ is strongly correlated to the maximum rain cell size and cell size spread (see Section 3), the cell size spread and maximum cell size increases with an increase in P. This fits observations by Trivej and Stevens (2010) from the RICO campaign, who highlight that especially large cells at the tail of the size distribution vary with precipitation area, which, we confirm, determines to a first order the precipitation amount. We find that, on average, the 20% largest cells in a scene have a mean cell size 2.5 times larger than the mean scene cell size and contribute half to the precipitating area and 60% to the precipitation amount. This contribution increases up to 70% in the 10% of rainiest scenes (not shown). That is, as the amount of precipitation in a scene increases, the precipitation is distributed more unevenly across the cells.

Recalling our previous analyses, we notice that P varies differently as a function of $\overline{S}$ and N than I_{ORG}. This is clear when comparing P and I_{ORG} in the $\overline{S}$–N phase space (Figure 8c) and is shown in a more condensed form in Figure 10, which aggregates the dominant relationships between precipitation amount and cell size, number, and arrangement. Figure 10 shows that P increases with $\overline{S}$ or N, but I_{ORG} does not. At large N, I_{ORG} is systemically lower than at small N and decreases with $\overline{S}$. Though precipitation amount maximizes at large N and $\overline{S}$, the degree of clustering minimises here, suggesting both are negatively correlated with each other. This is also indicated by contours of P and I_{ORG} in the upper part of the $\overline{S}$–N phase space (Figure 8c), which tend to be roughly parallel. At small N, however, I_{ORG} increases with $\overline{S}$ (Figure 10), so that in the lower part of the $\overline{S}$–N phase space (Figure 8c) the contours of P and I_{ORG} are perpendicular to each other, suggesting they vary independently. Across the whole dataset, the relationship between precipitation amount and clustering is therefore negative but foremost weak ($R = -0.41$, Figure 4). Consequently, precipitation amounts can be similar for scenes with a quite different spatial structure (Figure 10)—with rather many, small and weakly clustered cells or few, large and more strongly clustered cells (see also Figure 8c).

These analyses hence suggest that hypothesised mechanisms, such as that clustering increases precipitation through cell interaction, play overall no or a subordinate role for the precipitation amount in a scene, because precipitation amount increases with rain fraction and maximises when cells are large and numerous, whereas the degree of clustering maximises when cells are large but few. We find that scenes with small N and large $\overline{S}$, which show on average a high degree of clustering, also contribute little to the total observed precipitation amount (Figure 8d). This suggests that scenes with a high degree of clustering neither precipitate the most nor occur frequently enough to contribute much to the precipitation amount; hence, the spatial arrangement of rain cells is of second-order importance for precipitation amount in the trades. Similar conclusions were drawn for deep convection (e.g., Brueck *et al.*, 2020; Pscheidt *et al.*, 2019).

Only when considering the moisture environment may a positive effect of clustering on precipitation amounts be seen. Combining the results of Figure 8b and 8c, at small N in the dry regime, precipitation amount is higher for scenes with larger $\overline{S}$ and a higher degree of clustering. Further, keeping precipitation amount constant while moving in the $\overline{S}$–N phase space into scenes with small N, which tend to be dry, an increase in the mean cell size and an increase in the degree of clustering take place (see also Figure 10). In this sense, clustering may be considered

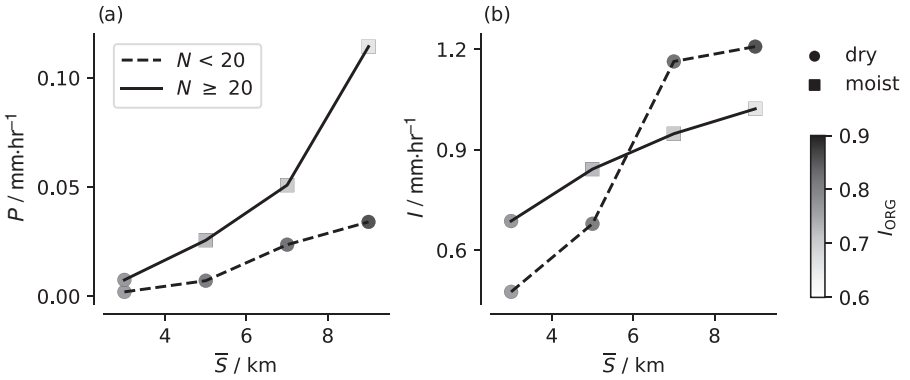

FIGURE 10 Overview of relationships between precipitation characteristics and cell number, size, and arrangement. (a) Precipitation amount P and (b) precipitation intensity I for bins of mean cell size $\overline{S}$ conditioned on different cell numbers N. The marker shading denotes the cells' degree of clustering as quantified by the I_{ORG} and the the moisture environment as quantified by $W \lesseqgtr 36\,\mathrm{kg\cdot m^{-2}}$

important for maintaining precipitation amounts in dry environments, as similarly found by Brueck *et al.* (2020) for deep convection.

4.2 | Precipitation intensity

We analyse the relationship between precipitation intensity, cell number, and mean cell size using the $\overline{S}$–N phase space. Figure 8e shows that I increases with $\overline{S}$ for a given N. For a given $\overline{S}$, I does not systematically increase or decrease with N (see also Figure 10). Consequently, the positive correlation between I and N across the whole dataset ($R = 0.39$, Figure 4) is due to an increase of I with $\overline{S}$ ($R = 0.52$, Figure 4) and the covariation of N with S ($R = 0.61$, Figure 4). Whereas both cell number and size are important for the precipitation amount in the trades, it seems predominantly the latter for precipitation intensity. This was similarly found in regimes of deep tropical convection (Louf *et al.*, 2019; Semie and Bony, 2020) and is, for example, important for cumulus parametrisations, where the convective area is a key ingredient. Whereas the convective or precipitating area well describes the precipitation amount, its composition into cell size and number is decisive for precipitation intensity.

Possible explanations for why precipitation intensity increases with mean cell size are that large cells protect their updrafts better from dilution by entrainment, which allows them to sustain stronger updrafts and grow deeper (e.g., Kirshbaum and Grant, 2012; Schlemmer and Hohenegger, 2014). Additionally, enhanced moisture aggregation through shallow circulations that accompany large clusters (Bretherton and Blossey, 2017) could increase the liquid and rain water content. Also, large cells may dissipate more slowly; that is, they live longer, and therefore develop a moister (sub)cloud layer that leads to less evaporation of the falling raindrops. Here, we can only provide a quantification of this effect. To do so, we investigate how the rain intensity of an individual

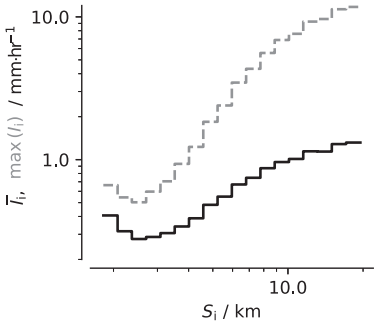

FIGURE 11 Mean intensity $\overline{I}_i$ (solid) and maximum intensity $\max(I_i)$ (dashed) of a cell binned as a function of cell size

cell scales with its size, shown in Figure 11 for the mean and maximum rain intensity of a cell. Both maximum and mean rain intensity increase with cell size for cell sizes above 3 km. Cells with a size around 10 km have a mean intensity around $1\,\mathrm{mm\cdot hr^{-1}}$. A maximum intensity above $1\,\mathrm{mm\cdot hr^{-1}}$ occurs in cells larger than roughly 5 km. As roughly 50% of cells are larger than 5 km (see Section 3.1), roughly 50% of the cells exhibit maximum intensities above $1\,\mathrm{mm\cdot hr^{-1}}$, a threshold associated with the formation of cold pools in past studies (e.g., Barnes and Garstang, 1982, Drager and van den Heever, 2017).

The analysis of I in the $\overline{S}$–N phase space further shows that the increase of I with $\overline{S}$ differs between small and large N (Figure 8e), more explicitly shown in Figure 10. In scenes with small N, the increase of I with $\overline{S}$ is stronger than in scenes with large N. This could indicate that cells are competing for moisture and heat—when there are many cells, they can grow larger, but not as intense as if there are few cells, because they have to compete with many cells. We identified a moist regime at large N and a dry regime at small N (Section 3.2), suggesting that I increases more strongly with $\overline{S}$ in dry compared with moist scenes and that precipitation intensities are thus highest in dry scenes. Figure 12 confirms this. The distribution of precipitation intensities in dry scenes shows a higher

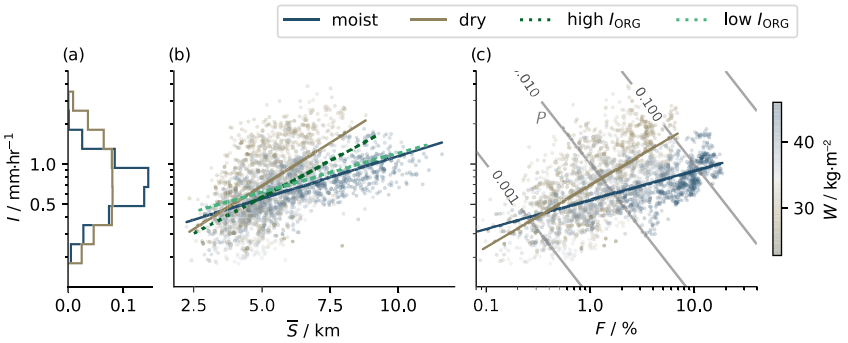

FIGURE 12 a) Relative frequency of precipitation intensity I for dry ($W >$ median (W)) and wet scenes ($W <$ median (W)). I as a function of (b) mean cell size $\overline{S}$ and (c) rain fraction F. The shading in (b) and (c) denotes the water vapour path W. The lines in (b) and (c) denote the fit for dry and wet scenes or scenes with high I_{ORG} ($I_{ORG} >$ p75 (I_{ORG})) and low I_{ORG} ($I_{ORG} <$ p25 (I_{ORG})). The slanted grey lines labelled P denote the precipitation amount in mm·hr^{-1} [Colour figure can be viewed at wileyonlinelibrary.com]

variability and extends to larger values than in moist scenes. Precipitation intensity is highest in dry environments, which was similarly observed by Louf *et al.* (2019) for deep convection. Vogel *et al.* (2020) also find that, in dry environments, simulated shallow clouds are deeper. Because I increases with $\overline{S}$ and maximises in dry environments, precipitation amount increases for the same rain fraction when moving from a moist environment with more numerous cells to a dry environment with larger cells (Figure 12c).

Our previous analyses show that dry and moist scenes also typically exhibit differences in the degree of clustering. We found that dry scenes are typically more clustered than moist scenes, and more clustered convection may help to let the clouds grow deeper and rain more intense, possibly adding to the enhanced increase of precipitation intensity with cell size in dry scenes. Figure 12 shows that the increase of I with $\overline{S}$ is stronger in scenes with a high degree of clustering than in scenes with a low degree of clustering. This suggests that high precipitation intensities are related to scenes with a high degree of clustering. Comparing the variations of precipitation intensity and clustering in the $\overline{S}$–N phase space (Figure 8e) or Figure 10, this is confirmed. At large N or moist environments, I increases with $\overline{S}$, whereas I_{ORG} decreases with $\overline{S}$. At small N or in dry environments, both I and I_{ORG} increase with $\overline{S}$. Thus, both I and I_{ORG} maximise where $\overline{S}$ is large and N is small (see also Figure 9c,f) and scenes are dry. The analyses hence suggest that clustering is important for high precipitation intensities occurring typically in dry environments. For a given mean cell size around 7 km, I and the degree of clustering increase as one moves from scenes with large N in the moist regime to scenes with a small N in the dry regime (Figure 10). Overall, however, I and I_{ORG} vary mostly perpendicular to each other in the $\overline{S}$–N phase space (Figure 8e), so that across all regimes the correlation between clustering and precipitation intensity is weak ($R = -0.18$, Figure 4).

5 | DIURNAL CYCLE

Our analysis so far takes a snapshot view of precipitation. To probe the evolution of the rain cells' spatial organisation, we lastly look at the diurnal cycle, a prominent mode of variability in the Tropics, revisited recently by Vial *et al.* (2019). This also allows us to add some context to our results by discussing our analyses of precipitation patterns in light of the analyses of cloud patterns in the diurnal cycle (Vial *et al.*, 2021; Vogel *et al.*, 2021). Measurements from the RICO field experiment show that trade-wind convection exhibits a night-time to early morning peak and an afternoon minimum in precipitation (Nuijens *et al.*, 2009; Snodgrass *et al.*, 2009), confirmed by the analyses of Vial *et al.* (2019). Figure 13 shows this daily cycle captured in our dataset with precipitation amount peaking in the early morning and having its minimum in the late afternoon before sunset (Figure 13a). Please note that the diurnal cycle is not complete on all days due to gaps in the measurements. Considering only the days with no gaps in the measurements, the diurnal cycle is similar.

The diurnal cycle of cell number and size roughly follow the diurnal cycle of precipitation amount (Figure 13c,d), which matches our previous analyses (Section 4). Thereby, N tends to peak before $\overline{S}$, suggesting that the increase in precipitation in the night is initially driven by more cells, then increasingly by larger cells. As N peaks, rain cells exhibit a low degree of clustering (Figure 13e). $\overline{S}$ stays high as N already decreases. This indicates that small cells might dissipate earlier whereas large cells live longer and/or that merging of cells are enhanced. Cells are now spaced close to each other, indicated by a large I_{ORG}. The early daytime between 0800 h and 1200 h, where $\overline{S}$ slowly decreases and I_{ORG} is high, is also characterised by a relatively high precipitation intensity (Figure 13b). Precipitation intensity does not show a clear

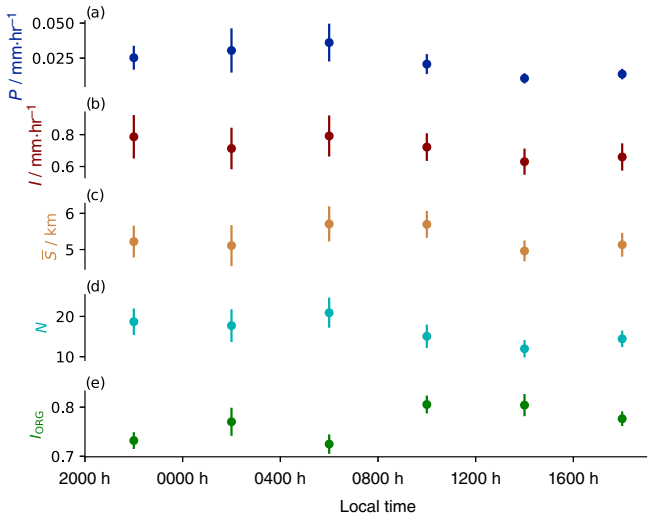

FIGURE 13 Mean diurnal cycle of (a) precipitation amount P, (b) precipitation intensity I, (c) cell number N, (d) mean cell size $\overline{S}$, and (e) the cells' spatial arrangement quantified by the I_{ORG}. Local time is UTC - 4h. Error bars denote the uncertainty in the mean (standard error) [Colour figure can be viewed at wileyonlinelibrary.com]

diurnal cycle. Vogel *et al.* (2021) find that cold pools prolong the peak in the diurnal cycle of precipitation into the early afternoon, possibly shaping this behaviour seen here.

Vial *et al.* (2021) show how the subjectively defined cloud patterns gravel, flowers, and fish (Stevens *et al.*, 2020) vary in the diurnal cycle. Please note that these cloud patterns extend in part over a larger scale than the ones analysed here. We may capture the gravel pattern, but only the individual rain cells of a single flower and a part of the fish pattern. Vial *et al.* (2021) show that the gravel cloud pattern has a peak occurrence around midnight, where we find rain cells to be rather small, numerous, and weakly clustered. Flowers, the appearance of which is mainly dominated through a large mean cloud size (Bony *et al.*, 2020), have a peak occurrence before sunrise, where we also find rain cells to be rather larger, and fish has a peak occurrence around noon, where we find rain cells to be rather large and strongly clustered. This might indicate that precipitation patterns and cloud patterns scale with each other. Figure 13 shows that the relationships revealed by our previous analyses are evident on the diurnal time scale and indicates how the number, size, and spatial arrangement of rain cells might relate to cloud patterns and the cells' life cycle.

6 | SUMMARY AND CONCLUSION

This study investigates the spatial behaviour of precipitating trade-wind convection and its implications for precipitation characteristics in the trades as observed during the EUREC^{4}A field campaign. To do so, scenes of trade-wind convection scanned by the C-band radar Poldirad are examined. We investigate the spatial structure in these scenes by analysing the size, number, and spatial arrangement of rain cells and examine how these relate to the scene's precipitation amount and intensity, as well as the water vapour path. A synopsis of the dominant relationships is given in Figure 10 and is summarised in the following.

During EUREC^{4}A, a mean rain cell size of 5 km and a mean distance to the nearest neighbour of about 14 km were most common. Up to 60 cells in one scene and a mean cell size of 12 km were observed. In nearly all scenes, cells were spaced closer than in a random distribution. That is, the spatial arrangement in scenes of precipitation is almost always clustered, which is in line with the expectation that precipitation is related to inhomogeneities. In the diurnal cycle, cell number tends to peak shortly before mean cell size in the early morning, and before the degree of clustering, which peaks around noon. Whereas cell number and mean size are positively correlated and cell number and clustering are negatively correlated, the relationship between mean cell size and clustering is more ambiguous and differs between scenes with a large and small cell number. Scenes with few and, on average, large cells exhibit typically the highest degree of clustering, which was similarly found for deep convection (Brueck *et al.*, 2020; Retsch *et al.*, 2020; Senf *et al.*, 2019). This suggests similarities between the spatial organisation of shallow and deep precipitating convection. Based on the diurnal cycle, we find indications that trade-wind precipitation patterns may scale with cloud patterns, providing a first observational baseline to study the relationship between the spatial organisation of precipitation and clouds.

We identify two regimes: a moist regime that is characterised by a large cell number, and a dry regime that generally has a small cell number. In the dry regime, cells are typically more clustered than in the moist regime, which agrees with deep convective studies (Bretherton *et al.*, 2005; Muller and Held, 2012; Tobin *et al.*, 2012). Clustering might reduce the updraft buoyancy reduction through entrainment, allowing cells to develop in hostile, dry environments (Becker *et al.*, 2018). Though we find a systematic relationship between water vapour path, cell number, and the degree of clustering, the relationship between water vapour path and cell size is less clear. Regarding the close relationship between water vapour availability and precipitation in the trades highlighted in Nuijens *et al.* (2009), our analyses suggest that precipitation increases with water vapour path predominantly because of more numerous cells that are more scattered rather than larger cells.

We conclude that the amount and intensity of precipitation behave differently to the spatial patterning in trade wind precipitation fields:

- The amount of precipitation varies closely with cell number and mean cell size because it scales well with rain fraction. High precipitation amounts typically occur in scenes that contain many, on average, large and weakly clustered cells. Precipitation amounts can be similar for scenes that differ markedly in their spatial structure.
- The intensity of precipitation increases predominantly with mean cell size. In dry scenes with few cells, this increase is stronger than in moist scenes with many cells. High precipitation intensities typically occur in dry scenes that contain, on average, large, few, and strongly clustered cells.

From the three spatial attributes investigated, cell size and number are equally strongly related to precipitation amount, and cell size is best related to precipitation intensity, thus highlighting the importance of cell size for precipitation characteristics. No causality can be derived from these relationships, though. Clustering and precipitation characteristics are, across all regimes, negatively and predominantly weakly correlated, and hence the spatial arrangement of cells is of second-order importance for precipitation in the trades. This was similarly noted for deep convection (e.g., Brueck *et al.*, 2020; Pscheidt *et al.*, 2019). We do find indications, however, that clustering may be important for high precipitation intensities and to maintain precipitation amounts in dry environments. Our study shows that precipitation characteristics are related to spatial precipitation patterns and suggests that a better understanding of how spatial patterns are conditioned on the environment (e.g., ambient moisture) will contribute to our understanding of precipitation in the trades.

ACKNOWLEDGEMENTS

This research was funded by the Deutsche Forschungsgemeinschaft (DFG, German Research Foundation) under Germany's Excellence Strategy—EXC 2037 'CLICCS—Climate, Climatic Change, and Society'—project number: 390683824, contribution to the Center for Earth System Research and Sustainability (CEN) of Universität Hamburg. We would like to thank Raphaela Vogel for valuable comments on the draft. We also thank the editors, Andrew Ross and Anthony Illingworth, as well as Louise Nuijens and two anonymous reviewers, for providing insightful feedback. The authors declare no conflict of interest. The data used in this publication were gathered in the EUREC^{4}A field campaign and are published by Hagen *et al.* (2021) and Bock *et al.* (2021) and available on the EUREC^{4}A AERIS database via https://doi.org/10.25326/217 and https://doi.org/10.25326/79. EUREC^{4}A is funded with support of the European Research Council, the Max Planck Society, the DFG, the German Meteorological Weather Service, and the German Aerospace Center.

AUTHOR CONTRIBUTIONS

Jule Radtke: conceptualization; formal analysis; visualization; writing – original draft. **Ann Kristin Naumann:** conceptualization; funding acquisition; supervision; writing – review and editing. **Martin Hagen:** data curation; investigation; writing – review and editing. **Felix Ament:** conceptualization; funding acquisition; supervision; writing – review and editing.

ORCID

Jule Radtke https://orcid.org/0000-0002-0387-5860

REFERENCES

Barnes, G.M. and Garstang, M. (1982) Subcloud layer energetics of precipitating convection. *Monthly Weather Review*, 110, 102–117. https://doi.org/10.1175/1520-0493(1982)110<0102:SLEOPC>2.0.CO;2.

Becker, T., Bretherton, C.S., Hohenegger, C. and Stevens, B. (2018) Estimating bulk entrainment with unaggregated and aggregated convection. *Geophysical Research Letters*, 45, 455–462. https://doi.org/10.1002/2017GL076640.

Betts, A.K. and Smith, R.K. (Ed.) (1997) Trade cumulus: Observations and modelling, *The physics and parameterization of moist atmospheric convection* (pp. 99–126). Dordrecht, Netherlands: Springer, https://doi.org/10.1007/978-94-015-8828-7_4.

Bock, O., Bosser, P., Flamant, C., Doerflinger, E., Jansen, F., Fages, R., Bony, S. and Schnitt, S. (2021) Integrated water vapour observations in the Caribbean arc from a network of ground-based GNSS receivers during EUREC^{4}A. *Earth System Science Data*, 13, 2407–2436. https://doi.org/10.5194/essd-13-2407-2021.

Bony, S. and Dufresne, J.-L. (2005) Marine boundary layer clouds at the heart of tropical cloud feedback uncertainties in climate models. *Geophysical Research Letters*, 32. https://doi.org/10.1029/2005GL023851.

Bony, S., Schulz, H., Vial, J. and Stevens, B. (2020) Sugar, gravel, fish, and flowers: Dependence of mesoscale patterns of trade-wind clouds on environmental conditions. *Geophysical Research Letters*, 47, L20806. https://doi.org/10.1029/2019GL085988.

Bony, S., Stevens, B., Ament, F., Bigorre, S., Chazette, P., Crewell, S., Delanoë, J., Emanuel, K., Farrell, D., Flamant, C., Gross, S., Hirsch, L., Karstensen, J., Mayer, B., Nuijens, L., Ruppert, J.H., Sandu, I., Siebesma, P., Speich, S., Szczap, F., Totems, J., Vogel, R., Wendisch, M. and Wirth, M. (2017) EUREC^{4}A: A field campaign to elucidate the couplings between clouds, convection and circulation. *Surveys in Geophysics*, 38, 1529–1568.

Bretherton, C.S. and Blossey, P.N. (2017) Understanding mesoscale aggregation of shallow cumulus convection using large-eddy simulation. *Journal of Advances in Modeling Earth Systems*, 9, 2798–2821.

Bretherton, C.S., Blossey, P.N. and Khairoutdinov, M. (2005) An energy-balance analysis of deep convective self-aggregation above uniform SST. *Journal of the Atmospheric Sciences*, 62, 4273–4292. https://doi.org/10.1175/JAS3614.1.

Bretherton, C.S., Peters, M.E. and Back, L.E. (2004) Relationships between water vapor path and precipitation over the tropical oceans. *Journal of Climate*, 17, 1517–1528. https://doi.org/10.1175/1520-0442(2004)017<1517:RBWVPA>2.0.CO;2.

Brueck, M., Hohenegger, C. and Stevens, B. (2020) Mesoscale marine tropical precipitation varies independently from the spatial arrangement of its convective cells. *Quarterly Journal of the Royal Meteorological Society*, 146, 1391–1402. https://doi.org/10.1002/qj.3742.

Denby, L. (2020) Discovering the importance of mesoscale cloud organization through unsupervised classification. *Geophysical Research Letters*, 47, 1–10.

Drager, A.J. and van den Heever, S.C. (2017) Characterizing convective cold pools. *Journal of Advances in Modeling Earth Systems*, 9, 1091–1115. https://doi.org/10.1002/2016MS000788.

Hagen, M., Ewald, F., Groß, S., Oswald, L., Farrell, D.A., Forde, M., Gutleben, M., Heumos, J., Reimann, J., Tetoni, E., Köcher, G., Marinou, E., Kiemle, C., Li, Q., Chewitt-Lucas, R., Daley, A., Grant, D. and Hall, K. (2021) Deployment of the C-band radar Poldirad on Barbados during EUREC^{4}A. *Earth System Science Data*, 13, 5899–5914. https://doi.org/10.5194/essd-13-5899-2021.

Kirshbaum, D.J. and Grant, A.L.M. (2012) Invigoration of cumulus cloud fields by mesoscale ascent. *Quarterly Journal of the Royal Meteorological Society*, 138, 2136–2150. https://doi.org/10.1002/qj.1954.

Lau, K.M. and Wu, H.T. (2003) Warm rain processes over tropical oceans and climate implications. *Geophysical Research Letters*, 30, 2–6.

Louf, V., Jakob, C., Protat, A., Bergemann, M. and Narsey, S. (2019) The relationship of cloud number and size with their large-scale environment in deep tropical convection. *Geophysical Research Letters*, 46, 9203–9212.

Marshall, J.S., Hitschfeld, W. and Gunn, K.L.S. (1955) Advances in radar weather. In H.E. Landsberg (Ed.), *Advances in geophysics* (Vol. 2 pp. 1–56): Elsevier, https://doi.org/10.1016/S0065-2687(08)60310-6.

Muller, C.J. and Held, I.M. (2012) Detailed Investigation of the self-aggregation of convection in cloud-resolving simulations. *Journal of the Atmospheric Sciences*, 69, 2551–2565. https://doi.org/10.1016/S0065-2687(08)60310-6.

Nuijens, L., Stevens, B. and Siebesma, A.P. (2009) The environment of precipitating shallow cumulus convection. *Journal of the Atmospheric Sciences*, 66, 1962–1979. https://doi.org/10.1175/2008JAS2841.1.

Pscheidt, I., Senf, F., Heinze, R., Deneke, H., Trömel, S. and Hohenegger, C. (2019) How organized is deep convection over Germany?. *Quarterly Journal of the Royal Meteorological Society*, 145, 2366–2384.

Rasp, S., Schulz, H., Bony, S. and Stevens, B. (2020) Combining crowdsourcing and deep learning to explore the mesoscale organization of shallow convection. *Bulletin of the American Meteorological Society*, 101, E1980–E1995. https://doi.org/10.1175/BAMS-D-19-0324.1.

Rauber, R.M., Stevens, B., Ochs, H.T., Knight, C., Albrecht, B.A., Blyth, A.M., Fairall, C.W., Jensen, J.B., S. G. Lasher-Trapp, O. L. Mayol-Bracero, G. Vali, J. R. Anderson, B. A. Baker, A. R. Bandy, E. Burnet, J.-L. Brenguier, W. A. Brewer, P. R. A. Brown, R. Chuang, W. R. Cotton, L. Di Girolamo, B. Geerts, H. Gerber, S. Göke, L. Gomes, B. G. Heikes, J. G. Hudson, P. Kollias, R. R. Lawson, S. K. Krueger, D. H. Lenschow, L. Nuijens, D. W. O'Sullivan, R. A. Rilling, D. C. Rogers, A. P. Siebesma, E. Snodgrass, J. L. Stith, D. C. Thornton, S. Tucker, C. H. Twohy and P. Zuidema (2007) Rain in shallow cumulus over the ocean: The RICO campaign. *Bulletin of the American Meteorological Society*, 88, 1912–1928. https://doi.org/10.1175/BAMS-88-12-1912.

Retsch, M.H., Jakob, C. and Singh, M.S. (2020) Assessing convective organization in tropical radar observations. *Journal of Geophysical Research: Atmospheres*, 125. https://doi.org/10.1029/2019JD031801.

Rieck, M., Nuijens, L. and Stevens, B. (2012) Marine boundary layer cloud feedbacks in a constant relative humidity atmosphere. *Journal of the Atmospheric Sciences*, 69, 2538–2550.

Schlemmer, L. and Hohenegger, C. (2014) The formation of wider and deeper clouds as a result of cold-pool dynamics. *Journal of the Atmospheric Sciences*, 71, 2842–2858. https://doi.org/10.1175/JAS-D-13-0170.1.

Schroth, A.C., Chandra, M.S. and Meischner, P.F. (1988) A C-band coherent polarimetric radar for propagation and cloud physics research. *Journal of Atmospheric and Oceanic Technology*, 5, 803–822.

Schulz, H., Eastman, R. and Stevens, B. (2021) Characterization and evolution of organized shallow convection in the downstream North Atlantic trades. *Journal of Geophysical Research: Atmospheres*, 126, e2021JD034575. https://doi.org/10.1029/2021JD034575.

Seifert, A. and Heus, T. (2013) Large-eddy simulation of organized precipitating trade wind cumulus clouds. *Atmospheric Chemistry and Physics*, 13, 5631–5645.

Semie, A.G. and Bony, S. (2020) Relationship between precipitation extremes and convective organization inferred from satellite observations. *Geophysical Research Letters*, 47, e2019GL086927. https://doi.org/10.1029/2019GL086927.

Senf, F., Brueck, M. and Klocke, D. (2019) Pair correlations and spatial statistics of deep convection over the tropical Atlantic. *Journal of the Atmospheric Sciences*, 76, 3211–3228.

Short, D.A. and Nakamura, K. (2000) TRMM radar observations of shallow precipitation over the tropical oceans. *Journal of Climate*, 13, 4107–4124.

Siebesma, A.P., Plate, E.J., Fedorovich, E.E., Viegas, D.X. and Wyngaard, J.C. (Eds.) (1998) Shallow cumulus convection, *Buoyant convection in geophysical flows* (pp. 441–486). Dordrecht, Netherlands: Springer, https://doi.org/10.1007/978-94-011-5058-3_19.

Siebesma, A.P., Bretherton, C.S., Brown, A., Chlond, A., Cuxart, J., Duynkerke, P.G., Jiang, H., Khairoutdinov, M., Lewellen, D., Moeng, C.-H., Sanchez, E., Stevens, B. and Stevens, D.E. (2003) A large eddy simulation intercomparison study of shallow cumulus convection. *Journal of the Atmospheric Sciences*, 60, 1201–1219. https://doi.org/10.1175/1520-0469(2003)60<1201:ALESIS>2.0.CO;2.

Smalley, K.M. and Rapp, A.D. (2020) The role of cloud size and environmental moisture in shallow cumulus precipitation. *Journal of Applied Meteorology and Climatology*, 59, 535–550.

Snodgrass, E.R., Di Girolamo, L. and Rauber, R.M. (2009) Precipitation characteristics of trade wind clouds during RICO derived from radar, satellite, and aircraft measurements. *Journal of Applied Meteorology and Climatology*, 48, 464–483.

Stevens, B. (2005) Atmospheric moist convection. *Annual Review of Earth and Planetary Sciences*, 33, 605–643.

Stevens, B., Bony, S., Brogniez, H., Hentgen, L., Hohenegger, C., Kiemle, C., L'Ecuyer, T.S., Naumann, A.K., Schulz, H., Siebesma, P.A., Vial, J., Winker, D.M. and Zuidema, P. (2020) Sugar, gravel, fish and flowers: Mesoscale cloud patterns in the trade winds. *Quarterly Journal of the Royal Meteorological Society*, 146, 141–152. https://doi.org/10.1002/qj.3662.

Stevens, B., Bony, S., Farrell, D., Ament, F., Blyth, A., Fairall, C., Karstensen, J., Quinn, P.K., Speich, S., Acquistapace, C., Aemisegger, F., Albright, A.L., Bellenger, H., Bodenschatz, E., Caesar, K.-A., Chewitt-Lucas, R., de Boer, G., Delanoë, J., Denby, L., Ewald, F., Fildier, B., Forde, M., George, G., Gross, S., Hagen, M., Hausold, A., Heywood, K.J., Hirsch, L., Jacob, M., Jansen, F., Kinne, S., Klocke, D., Kölling, T., Konow, H., Lothon, M., Mohr, W., Naumann, A.K., Nuijens, L., Olivier, L., Pincus, R., Pöhlker, M., Reverdin, G., Roberts, G., Schnitt, S., Schulz, H., Siebesma, A.P., Stephan, C.C., Sullivan, P., Touzé-Peiffer, L., Vial, J., Vogel, R., Zuidema, P., Alexander, N., Alves, L., Arixi, S., Asmath, H., Bagheri, G., Baier, K., Bailey, A., Baranowski, D., Baron, A., Barrau, S., Barrett, P.A., Batier, F., Behrendt, A., Bendinger, A., Beucher, F., Bigorre, S., Blades, E., Blossey, P., Bock, O., Böing, S., Bosser, P., Bourras, D., Bouruet-Aubertot, P., Bower, K., Branellec, P., Branger, H., Brennek, M., Brewer, A., Brilouet, P.-E., Brügmann, B., Buehler, S.A., Burke, E., Burton, R., Calmer, R., Canonici, J.-C., Carton, X., Cato, Jr.G., Charles, J.A., Chazette, P., Chen, Y., Chilinski, M.T., Choularton, T., Chuang, P., Clarke, S., Coe, H., Cornet, C., Coutris, P., Couvreux, F., Crewell, S., Cronin, T., Cui, Z., Cuypers, Y., Daley, A., Damerell, G.M., Dauhut, T., Deneke, H., Desbios, J.-P., Dörner, S., Donner, S., Douet, V., Drushka, K., Dütsch, M., Ehrlich, A., Emanuel, K., Emmanouilidis, A., Etienne, J.-C., Etienne-Leblanc, S., Faure, G., Feingold, G., Ferrero, L., Fix, A., Flamant, C., Flatau, P.J., Foltz, G.R., Forster, L., Furtuna, I., Gadian, A., Galewsky, J., Gallagher, M., Gallimore, P., Gaston, C., Gentemann, C., Geyskens, N., Giez, A., Gollop, J., Gouirand, I., Gourbeyre, C., de Graaf, D., de Groot, G.E., Grosz, R., Güttler, J., Gutleben, M., Hall, K., Harris, G., Helfer, K.C., Henze, D., Herbert, C., Holanda, B., Ibanez-Landeta, A., Intrieri, J., Iyer, S., Julien, F., Kalesse, H., Kazil, J., Kellman, A., Kidane, A.T., Kirchner, U., Klingebiel, M., Körner, M., Kremper, L.A., Kretzschmar, J., Krüger, O., Kumala, W., Kurz, A., L'Hégaret, P., Labaste, M., Lachlan-Cope, T., Laing, A., Landschützer, P., Lang, T., Lange, D., Lange, I., Laplace, C., Lavik, G., Laxenaire, R., Le Bihan, C., Leandro, M., Lefevre, N., Lena, M., Lenschow, D., Li, Q., Lloyd, G., Los, S., Losi, N., Lovell, O., Luneau, C., Makuch, P., Malinowski, S., Manta, G., Marinou, E., Marsden, N., Masson, S., Maury, N., Mayer, B., Mayers-Als, M., Mazel, C., McGeary, W., McWilliams, J.C., Mech, M., Mehlmann, M., Meroni, A.N., Mieslinger, T., Minikin, A., Minnett, P., Möller, G., Morfa Avalos, Y., Muller, C., Musat, I., Napoli, A., Neuberger, A., Noisel, C., Noone, D., Nordsiek, F., Nowak, J.L., Oswald, L., Parker, D.J., Peck, C., Person, R., Philippi, M., Plueddemann, A., Pöhlker, C., Pörtge, V., Pöschl, U., Pologne, L., Posyniak, M., Prange, M., Quiñones Meléndez, E., Radtke, J., Ramage, K., Reimann, J., Renault, L., Reus, K., Reyes, A., Ribbe, J., Ringel, M., Ritschel, M., Rocha, C.B., Rochetin, N., Röttenbacher, J., Rollo, C., Royer, H., Sadoulet, P., Saffin, L., Sandiford, S., Sandu, I., Schäfer, M., Schemann, V., Schirmacher, I., Schlenczek, O., Schmidt, J., Schröder, M., Schwarzenboeck, A., Sealy, A., Senff, C.J., Serikov, I., Shohan, S., Siddle, E., Smirnov, A., Späth, F., Spooner, B., Stolla, M.K., Szkółka, W., de Szoeke, S.P., Tarot, S., Tetoni, E., Thompson, E., Thomson, J., Tomassini, L., Totems, J., Ubele, A.A., Villiger, L., von Arx, J., Wagner, T., Walther, A., Webber, B., Wendisch, M., Whitehall, S., Wiltshire, A., Wing, A.A., Wirth, M., Wiskandt, J., Wolf, K., Worbes, L., Wright, E., Wulfmeyer, V., Young, S., Zhang, C., Zhang, D., Ziemen, F., Zinner, T. and Zöger, M. (2021) EUREC^{4}A. *Earth System Science Data*, 13, 4067–4119. https://doi.org/10.5194/essd-13-4067-2021.

Stevens, B., Farrell, D., Hirsch, L., Jansen, F., Nuijens, L., Serikov, I., Brügmann, B., Forde, M., Linne, H., Lonitz, K. and Prospero, J.M. (2016) The Barbados Cloud Observatory: Anchoring investigations of clouds and circulation on the edge of the ITCZ. *Bulletin of the American Meteorological Society*, 97, 735–754.

Tobin, I., Bony, S. and Roca, R. (2012) Observational evidence for relationships between the degree of aggregation of deep convection, water vapor, surface fluxes, and radiation. *Journal of Climate*, 25, 6885–6904.

Tompkins, A.M. and Semie, A.G. (2017) Organization of tropical convection in low vertical wind shears: Role of updraft entrainment. *Journal of Advances in Modeling Earth Systems*, 9, 1046–1068. https://doi.org/10.1002/2016MS000802.

Touzé-Peiffer, L., Vogel, R. and Rochetin, N. (2022) Cold pools observed during EUREC^{4}A: detection and characterization from atmospheric soundings. *Journal of Applied Meteorology and Climatology*. https://doi.org/10.1175/JAMC-D-21-0048.1.

Trivej, P. and Stevens, B. (2010) The echo size distribution of precipitating shallow cumuli. *Journal of the Atmospheric Sciences*, 67, 788–804.

van Zanten, M.C., Stevens, B., Nuijens, L., Siebesma, A.P., Ackerman, A.S., Burnet, F., Cheng, A., Couvreux, F., Jiang, H., Khairoutdinov, M., Kogan, Y., Lewellen, D.C., Mechem, D., Nakamura, K., Noda, A., Shipway, B.J., Slawinska, J., Wang, S. and Wyszogrodzki, A. (2011) Controls on precipitation and cloudiness in simulations of trade-wind cumulus as observed during RICO. *Journal of Advances in Modeling Earth Systems*, 3, M06001. https://doi.org/10.1029/2011MS000056.

Vial, J., Dufresne, J.L. and Bony, S. (2013) On the interpretation of inter-model spread in CMIP5 climate sensitivity estimates. *Climate Dynamics*, 41, 3339–3362.

Vial, J., Vogel, R., Bony, S., Stevens, B., Winker, D.M., Cai, X., Hohenegger, C., Naumann, A.K. and Brogniez, H. (2019) A new look at the daily cycle of trade wind cumuli. *Journal of Advances in Modeling Earth Systems*, 11, 3148–3166.

Vial, J., Vogel, R. and Schulz, H. (2021) On the daily cycle of mesoscale cloud organization in the winter trades. *Quarterly Journal of the Royal Meteorological Society*, 147, 2850–2873.

Villiger, L., Wernli, H., Boettcher, M., Hagen, M. and Aemisegger, F. (2022) Lagrangian formation pathways of moist anomalies in the trade-wind region during the dry season: Two case studies from EUREC^{4}A. *Weather and Climate Dynamics*, 3, 59–88. https://doi.org/10.5194/wcd-3-59-2022.

Vogel, R., Konow, H., Schulz, H. and Zuidema, P. (2021) A climatology of trade-wind cumulus cold pools and their link to mesoscale cloud organization. *Atmospheric Chemistry and Physics*, 21, 16609–16630. https://doi.org/10.5194/acp-21-16609-2021.

Vogel, R., Nuijens, L. and Stevens, B. (2016) The role of precipitation and spatial organization in the response of trade-wind clouds to warming. *Journal of Advances in Modeling Earth Systems*, 8, 843–862. http://doi.wiley.com/10.1002/2015MS000568.

Vogel, R., Nuijens, L. and Stevens, B. (2020) Influence of deepening and mesoscale organization of shallow convection on stratiform cloudiness in the downstream trades. *Quarterly Journal of the Royal Meteorological Society*, 146, 174–185. https://doi.org/10.1002/qj.3664.

Weger, R.C., Lee, J., Zhu, T. and Welch, R.M. (1992) Clustering, randomness and regularity in cloud fields: 1. Theoretical considerations. *Journal of Geophysical Research: Atmmospheres*, 97, 20519–20536.

White, B.A., Buchanan, A.M., Birch, C.E., Stier, P. and Pearson, K.J. (2018) Quantifying the effects of horizontal grid length and parameterized convection on the degree of convective organization using a metric of the potential for convective interaction. *Journal of the Atmospheric Sciences*, 75, 425–450.

Zuidema, P., Li, Z., Hill, R.J., Bariteau, L., Rilling, B., Fairall, C., Brewer, W.A., Albrecht, B. and Hare, J. (2012) On trade wind cumulus cold pools. *Journal of the Atmospheric Sciences*, 69, 258–280. https://doi.org/10.1175/JAS-D-11-0143.1.

How to cite this article: Radtke, J., Naumann, A.K., Hagen, M. & Ament, F. (2022) The relationship between precipitation and its spatial pattern in the trades observed during EUREC^{4}A. *Quarterly Journal of the Royal Meteorological Society*, 148(745), 1913–1928. Available from: https://doi.org/10.1002/qj.4284